Effect of Ga doping on glass-forming ability and mechanical properties of CuZrAlY metallic glass composites

Peng XUE, Kun QIAN, Xiao-bing LI, Bo CHEN, Lei SHU, Meng-shu ZHANG, Jun-jie HAO, Kui LIU

Department of Materials Science and Technology, Jihua Laboratory, Foshan 528000, China

Abstract: The influence of Ga doping on the structure and mechanical properties of $B2$-CuZr phase reinforced larger-size CuZrAlY metallic glass composites was investigated by experiments and simulations. The result showed that as Ga content increased, the glass-forming ability of CuZrAlY metallic glass composites was gradually enhanced. Section morphology and thermal analysis indicated that Ga doping induced the decreased content of the crystals and the enlargement of the super-cooled liquid region, and increased activation energy for crystallization. Ga also stabilized the $B2$-CuZr phase. Characterization of the microstructure and mechanical test results suggested that the $B19'$-CuZr phase disappeared in the as-cast samples after adding Ga, and the martensitic transformation of the $B2$-CuZr phase was hindered when Ga content increased. The evolution mechanism of mechanical behaviors of the CuZr-based metallic glass composites during Ga doping was clarified by first-principles calculation. The results would be beneficial to the development and application of large-size CuZr-based metallic glass composites.

Key words: metallic glass composite; alloying; thermal properties; mechanical properties; density functional theory

1 Introduction

Bulk metallic glasses (BMGs) with long-range disorder atomic configuration embody good mechanical properties, except poor plasticity at room temperature [1]. To suppress the brittle fracture and enhance the application safety of BMGs, ductile crystal phases are introduced into the glassy matrix, which creates metallic glass composites (MGCs) [2,3]. Among the MGCs, $B2$-CuZr phase reinforced CuZr-based MGCs attract great attention because of their outstanding deformability and pronounced work-hardening behavior along with high hardness and strength [4,5]. The excellent mechanical properties of the CuZr-based MGCs are derived from the intrinsic properties of CuZr-based BMGs and the stress-induced martensitic transformation of CsCl type $B2$-CuZr phase, which inhibits the strain-softening of the amorphous matrix [6−9].

However, rapid cooling of the alloy melt is the prerequisite to form CuZr-based MGCs, which limits the size of MGCs and then hinders further application. Although 3D printing, welding, and other methods are technically feasible solutions to acquire large-size MGCs [10−12], the $B2$-CuZr phase, a metastable phase below 723 °C, could decompose to brittle $CuZr_2$ and $Cu_{10}Zr_7$ phases or transform to martensitic $B19'$-CuZr phase during rapid heating and cooling [13]. Those structural changes of the crystal accompanied by the structural relaxation and the crystallization of the amorphous matrix may deteriorate the mechanical behavior of MGCs.

Large-size MGCs containing only $B2$-CuZr

phase reinforcement, which is possible to show good mechanical behavior [14], can be designed by microalloying [15]. SONG et al [16] proposed a feasible strategy to obtain the desired structure, which first improves the glass-forming ability (GFA) of the CuZr-based alloys and then induces heterogeneous nucleation of the $B2$-CuZr phase. Therefore, identifying the effect of a specific element on the structure and mechanical properties is significant to design the CuZr-based MGCs. In the recent two decades, it has been widely proved by experiments and simulations that the GFA of CuZr-based BMGs is increased after adding Al [17], Ag [18], Zn [19], and rare-earth [20], and the structural stability of the $B2$-CuZr phase is enhanced by introducing elements such as Fe [21,22], Co [18], and Sc [23] into the alloy. INOUE et al [24] reported that group IIIA elements B, Al, and Ga enlarged the composition range to form the amorphous phase in the CuZr alloy system. However, as an effective GFA-promoting element, more than 8 wt.% Al addition will facilitate the precipitation of AlZr intermetallic, rather than increase the GFA of CuZr-base BMGs [25]. Providing p-type electrons like Al- and Ga-doping may induce stronger bonding in the icosahedral-like CuZr clusters, which implies the elevated GFA [26,27]. Ga could also stabilize the $B2$-CuZr phase at room temperature, hindering the martensitic transformation in CuZrAl MGCs [28]. Those results suggest that Ga is beneficial to acquiring large-size $B2$-CuZr phase reinforced CuZr-based MGCs; however, a detailed study about the alloying effect of Ga on CuZr-based MGCs is still lacking.

In this work, Y was first added to enhance the GFA of $Cu_{47}Zr_{47}Al_6$ and guarantee the formation of large-size MGC [29], then the effect of Ga addition to CuZrAlY alloy on the GFA, structural stability of the amorphous phase and $B2$-CuZr phase, and the mechanical properties of CuZr-based MGCs was explored. As a result, centimeter-scale MGCs with single $B2$-CuZr phase reinforcement were synthesized, and the mechanism of the structural and mechanical behavior evolution of the Ga-doped MGCs was investigated by experiments and density functional theory (DFT) simulation. These findings would favor designing the composition, understanding the formation mechanism, and improving the mechanical properties of large-size CuZr-based MGCs.

2 Materials and methods

2.1 Experiments

Alloy ingots with the nominal composition of $(Cu_{50}Zr_{50})_{93-x}Al_6Y_1Ga_x$ (x=0, 0.5, 1.0, 1.5, and 2.0 in at.%) were fabricated in an arc-melting furnace with Ti-gettered Ar atmosphere. The chemical homogeneity of the ingots was guaranteed by 4 times remelting the mixture of high-purity elements (>99.9 wt.%). Using suction casting, rods with a diameter of 10 mm were prepared in a water-cooled copper mold. The section of the rods was observed with a Zeiss Axio Imager M2m optical microscope (OM). X-ray diffraction (XRD) using Cu $K_α$ radiation on Bruker D8 Advance and transmission electron microscopy (TEM) on Thermo-Fisher Scientific Talos F200X were employed to characterize the phases. The distribution of elements was determined by energy dispersive spectrometry (EDS) mapping in TEM. The as-cast samples were heated in a TA DSC 250 differential scanning calorimeter (DSC) to investigate the thermal properties at the heating rates of 5, 10, 20, and 40 °C/min. The microhardness was measured by the HVS−1000Z Vickers microhardness tester, the load was set to be 0.3 kg, and the holding time was 10 s. Compressive mechanical behaviors of the MGC samples with dimensions of 2 mm × 2 mm × 4 mm were measured by an MTS electromechanical test system with a strain rate of $5×10^{-4}\,s^{-1}$. To avoid casting defects, the samples were cut from the core of the as-cast rods and carefully polished before the tests.

2.2 Simulation

First-principles calculations were performed by a DFT-based Siesta code [30]. The pseudo-potentials in the PSML format were used to determine the interactions between the ions and electrons [31]. The exchange-correlation energy was calculated in Perdew−Burke−Ernzerhof (PBE) generalized gradient approximation [32]. Double-$ζ$ with polarization basis functions and only Γ-point sampling were used for the calculations. The mesh cutoff was set to be 200 Ry, which defines the real-space-grid spacing used to represent the charge densities and potentials. The initial $B2$-CuZr and $B19'$-CuZr supercells contained 250 and 256 atoms

with periodic boundary conditions, respectively. The amorphous model was constructed by heating and quenching the $B2$-CuZr supercell and then optimized using the conjugate gradient method. The VESTA program was used to visualize the structural and charge information after the calculations [33].

3 Results and discussion

3.1 Structures of Ga-doped CuZrAlY MGCs

Figure 1 exhibits the sectional morphologies of the $(Cu_{50}Zr_{50})_{93-x}Al_6Y_1Ga_x$ (x=0, 0.5, 1.0, 1.5, and 2.0 in at.%) MGCs, where the assembled images are used to display the entire section of the large-size samples. Two distinct regions can be distinguished in Fig. 1, the brighter matrix represents the amorphous matrix, and the darker precipitate is the crystal phase. Some crystals with diameters of 0.5−1 mm pointed by arrows are homogeneously embedded in the amorphous matrix, and the quantity of the crystals decreases when Ga content increases. Based on the empirical rules proposed by INOUE [34], Ga could be a candidate to enhance the GFA of CuZr alloy, because both the Ga−Zr and Ga−Y mixing enthalpies are −40 kJ/mol and the radius of Ga atom (1.35 Å) is between radius of Al atom (1.43 Å) and Cu atom (1.28 Å), significantly

smaller than the radius of Zr atom (1.60 Å) and Y atom (1.80 Å). The results in Fig. 1 confirm that Ga doping induces the increased GFA of CuZr-based MGCs.

XRD patterns of $(Cu_{50}Zr_{50})_{93-x}Al_6Y_1Ga_x$ (x=0, 0.5, 1.0, 1.5 and 2.0 in at.%) MGCs are shown in Fig. 2. Sharp peaks on all the patterns identified as the $B2$-CuZr phase are superimposed on the diffuse scattering maximum; however, peaks of the $B19'$-CuZr phase can only be found in the sample without Ga addition. As an equilibrium phase at elevated temperature, the $B2$-CuZr phase firstly crystallizes in the liquid and then decomposes into the $CuZr_2$ and $Cu_{10}Zr_7$ phases at 723 °C [13]. However, during the rapid cooling, the decomposition of the $B2$-CuZr phase is inhibited, and the $B2$-CuZr phase maintains its structure after the solidification of MGCs. At room temperature (RT), the $B2$-CuZr phase is metastable and tends to transform to the martensitic $B19'$-CuZr phase. Without Ga addition, martensitic transformation occurs before the sample is cooled to RT, whereas no $B19'$-CuZr phase is found in the Ga-doped samples. It is inferred that Ga addition induces the suppression of martensitic transformation of the $B2$-CuZr phase, i.e., enhances the stability of the $B2$-CuZr phase at RT, which is consistent with the results of ZHOU et al [28].
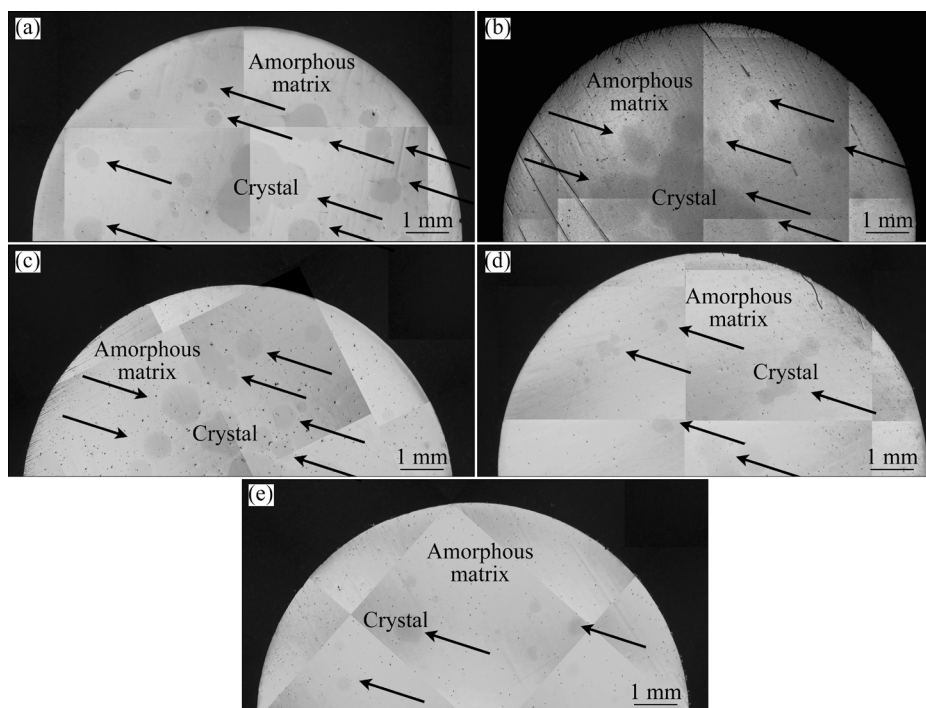

Fig. 1 Optical morphologies of CuZrAlYGa MGCs with different Ga contents: (a) 0 at.% Ga; (b) 0.5 at.% Ga; (c) 1.0 at.% Ga; (d) 1.5 at.% Ga; (e) 2.0 at.% Ga
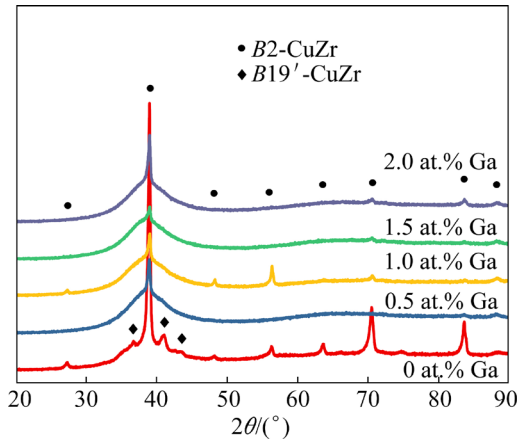
Fig. 2 XRD patterns of $(Cu_{50}Zr_{50})_{93-x}Al_6Y_1Ga_x$ (x=0, 0.5, 1.0, 1.5, 2.0, at.%) MGC samples

Figure 3 shows the TEM image of the $(Cu_{50}Zr_{50})_{92}Al_6Y_1Ga_1$ sample and the corresponding elements distribution. The interface between the featureless amorphous matrix and the $B2$-CuZr phase is shown in Fig. 3(a), and the diffraction halo and spots corresponding to the marked regions point out the structure of the $B2$-CuZr phase and the amorphous phase, respectively. Scanning the green line in Fig. 3(a) using EDS, the distribution of elements near the interface between the amorphous phase and the $B2$-CuZr phase is represented in Fig. 3(b). Although the sample holder made of Cu

induces a higher Cu fraction, no significant difference in the elemental content can be found near the phase interface marked by a dashed line in Fig. 3(b). Additionally, elemental mappings of Fig. 3(a) shown in Fig. 3(c) show no segregation in the sample, which suggests that rapid cooling hinders the diffusion of elements.

3.2 Thermal stability of amorphous matrix

From the DSC curves of the samples at a heating rate of 20 °C/min in Fig. 4(a), the glass transition temperature (T_g) and the crystallization temperature (T_x) are identified and listed in Table 1. The increasing crystallization temperature and width of the supercool liquid region (T_x-T_g) verify the enhanced GFA of the alloys after Ga-doping shown in Fig. 1. To further investigate the thermal stability of the amorphous phase, the activation energy for crystallization (E_a) is calculated using the Kissinger equation [35]:

$$\ln\left(\frac{B}{T_x^2}\right) = -\frac{E_a}{RT_x} + A$$

where B is the heating rate, R is the molar gas constant, and A is a constant. A Kissinger plot in Fig. 4(b) depicts $\ln(B/T_x^2)$ versus $1000/(RT_x)$ and the fitted lines, and then the slopes of the lines representing E_a are exhibited. The growing E_a from
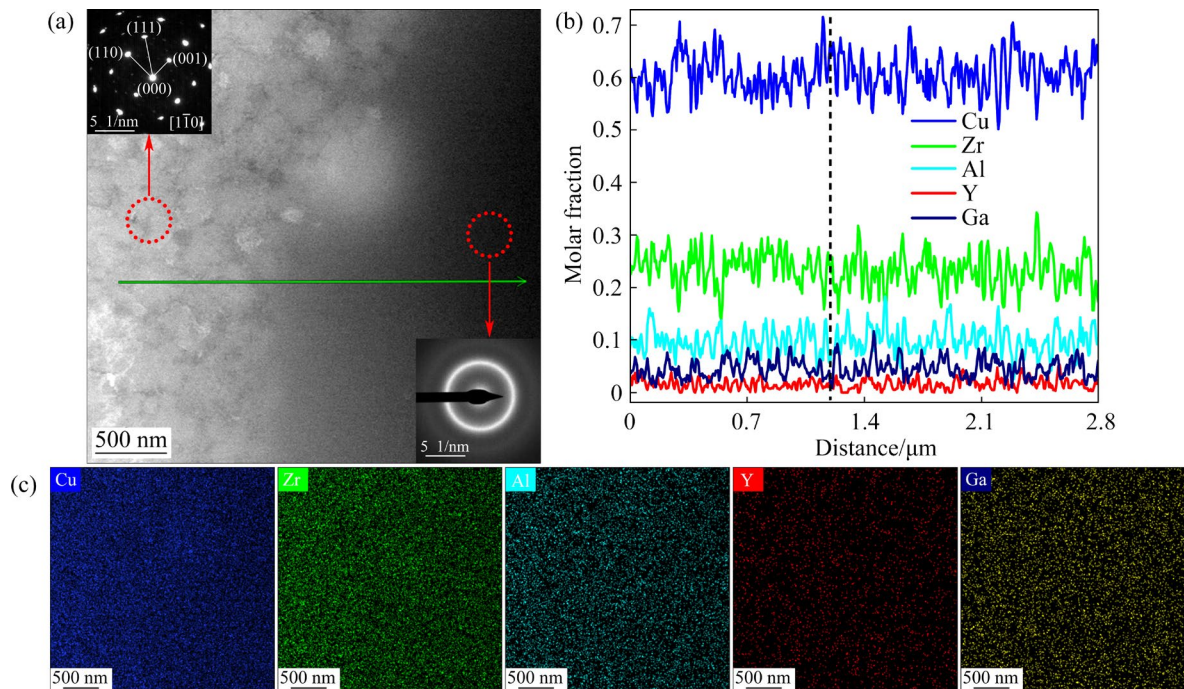

Fig. 3 TEM image of $(Cu_{50}Zr_{50})_{92}Al_6Y_1Ga_1$ MGC (a), corresponding EDS scan mapping (b) of green line in (a), and elemental mappings (c) of (a)
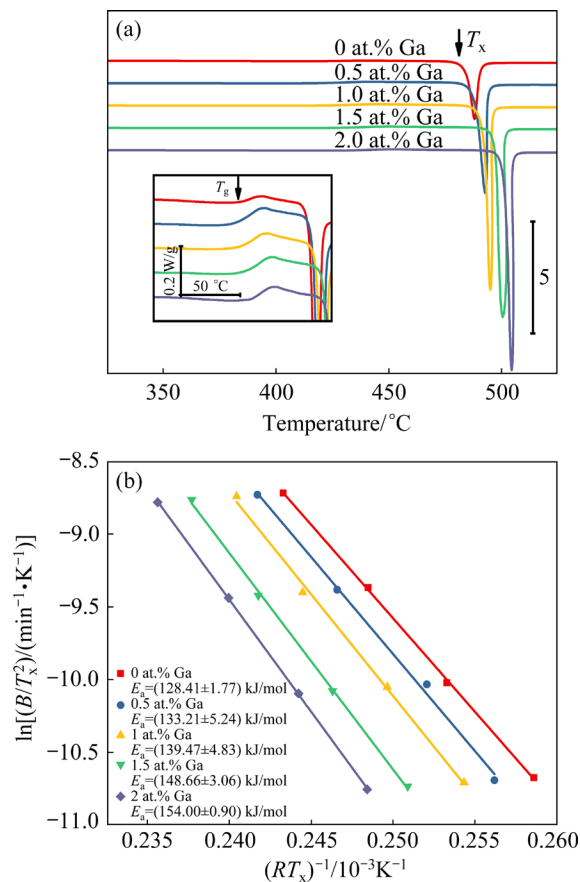
Fig. 4 DSC curves with heating rate of 20 °C/min and inset showing enlarged curves between 350 and 500 °C (a), and Kissinger plot of MGC samples (b)

Table 1 Thermal properties of MGC samples with heating rate of 20 °C/min

Ga content/at.%	T_g/°C	T_x/°C	(T_x-T_g)/°C
0	420	484	64
0.5	418	488	70
1.0	422	492	70
1.5	426	498	72
2.0	429	501	72

(128.41±1.77) to (154.00±0.9) kJ/mol indicates that the thermal stability of the amorphous phase in CuZrAlY MGCs is enhanced by Ga microalloying.

3.3 Mechanical properties of CuZrAlYGa MGCs

The mechanical behaviors including Vickers hardness and compressive deformation of MGCs in this work are shown in Fig. 5. Figure 5(a) illustrates Vickers hardness of the amorphous CuZr phase and the $B2$-CuZr phase. As Ga content increases, the amorphous matrix maintains the hardness between

HV (498.67±5.61) and HV (503.69±6.1), while the hardness of the $B2$-CuZr phase gradually increases from HV (370.32±9.73) to HV (385.29±9.07). Figure 5(b) depicts the compressive mechanical properties of MGCs. Although the fracture stress and strain are similar among the samples, the yield strength increases from 303.47 to 647.42 MPa with rising Ga content from 0 to 2.0 at.%, and the yield strain increases from 1.068% to 2.42% correspondingly. After yielding, all the samples show remarkable work-hardening, which is derived from the martensitic transformation of the $B2$-CuZr phase. The increased yield strength could stem from the decreasing content of the crystal caused by Ga addition (see Fig. 1) [23,36]. On the other hand, considering the hardening of the $B2$-CuZr phase, Ga doping may also hinder the martensitic transformation of the $B2$-CuZr phase and lead to higher yield strength. It should be noted here that the fracture occurs after the appearance of serrated yielding, i.e., the yield of the amorphous matrix. This indicates that the crystals with excessive size cannot suppress the rapid propagation of shear bands in the glassy matrix.
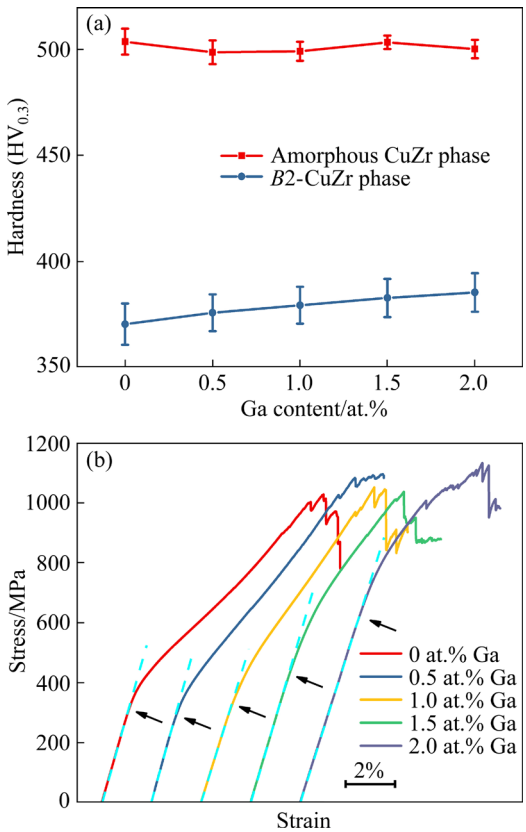

Fig. 5 Mechanical properties of MGC samples: (a) Vicker hardness of $B2$-CuZr and amorphous CuZr phases; (b) Compressive stress−strain curves

3.4 DFT simulation of Ga-doped CuZr phases

To better understand the evolution of microstructure and mechanical behavior of the Ga-doped MGCs, DFT calculation was employed. As shown in Fig. 3, Ga is homogeneously distributed in the MGC. In other words, the rapid cooling suppressed the migration of atoms, and Ga could occupy the position of Cu and Zr atoms randomly in the phases. Therefore, the models for pure $B2$-CuZr phase, $B19'$-CuZr phase, and amorphous CuZr phase were built and then some Cu and Zr atoms were equally replaced by Ga atoms in random to construct the Ga-doped model, which are shown in the inset of Fig. 6. The Ga content-related formation energy of the $B2$-CuZr phase, $B19'$-CuZr phase, and amorphous phase is illustrated in Fig. 6. For the $B2$-CuZr phase, the formation energy of the pure phase is −0.101 eV/atom, while the formation energy of the pure $B19'$-CuZr phase is −0.121 eV/atom, which indicates that the $B19'$-CuZr phase is relatively stable without Ga addition.
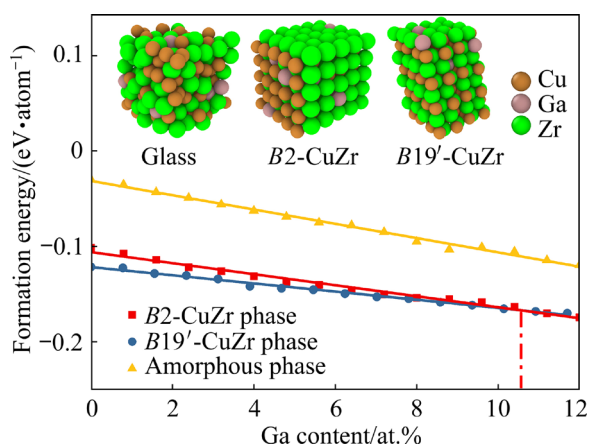

Fig. 6 Formation energy of Ga-doped $B2$-CuZr, $B19'$-CuZr, and amorphous CuZr phases

When Ga content increases from 0 to 12 at.%, the formation energy of $B2$-CuZr and $B19'$-CuZr phases decreases monotonically. The decreasing rate of formation energy of the $B2$-CuZr and $B19'$-CuZr phases is 0.00577 and 0.00428 eV/atom, respectively. The stabilization of the $B2$-CuZr phase may promote the precipitation in supercooled liquid and impede the decomposition. The faster formation energy reduction of the $B2$-CuZr phase along with more Ga doping causes decreasing driving force of martensite transformation. When the Ga content is greater than 10.5 at.%, $B2$-CuZr

phase is the most stable phase in the current system. However, in reality, the hydrostatic pressure [7,37] and the crystalline−amorphous phase interface [38] hinder the $B2{\rightarrow}B19'$ martensitic transformation in the CuZr-based MGCs, which reduces the critical Ga content for the stabilization of the $B2$-CuZr phase. These are the reasons for the disappearing peaks of the $B19'$-CuZr phase in the XRD patterns of Ga-added MGC samples in Fig. 2.

As a metastable phase with a disordered structure, the formation energy of the amorphous CuZr phase is −0.030 eV/atom, higher than that of the $B2$-CuZr phase and $B19'$-CuZr phase. The decreasing rate of formation energy of the amorphous CuZr phase is −0.00748 eV/atom when Ga content increases. The larger negative slope of the amorphous CuZr phase demonstrates the reducing driving force for the crystallization and then the amorphous CuZr phase is stabilized after Ga doping, which confirms the analysis results of Figs. 1 and 4.

The electronic density of states (DOS) of the Ga-doped $B2$-CuZr samples is calculated based on the model in Fig. 6. The total DOS (TDOS) and the projected DOS (PDOS) are plotted in Fig. 7(a), and the dashed line at zero energy reflects the Fermi level. The TDOS of the $B2$-CuZr phase is 257.95 states/eV at the Fermi level, which denotes the metallic character. The d orbitals of Cu and Zr elements dominate the bonding states below the Fermi level; meanwhile, the antibonding states are mainly contributed to Zr-d orbital. When Ga content increases to 4, 8, and 12 at.% in the $B2$-CuZr crystal, except for the rising PDOS peaks of Ga, the TDOS at the Fermi level decreases to 235.02, 227.63, and 215.11 states/eV, respectively. This suggests the weakening of the metallicity of the Ga-substituted $B2$-CuZr phase. For the $B2$-CuZr phase, the PDOS peaks of Cu-d and Zr-d from −5 to −2 eV overlap, indicating that the covalent bonding results from the interaction between Cu-d and Zr-d. When Ga is added to the system, the hybridization of Ga-p with Cu-s, Zr-s, and Zr-d from −7 to −3 eV indicates the enhancement of the covalent bonding.

Compared with the TDOS curves of the $B2$-CuZr phase, the DOS curves of the amorphous CuZr phase in Fig. 7(b) feature smoothness and decreased height of the peaks, which stems from the disordered structure and then the increased defects in the system. In the view of PDOS, the states of
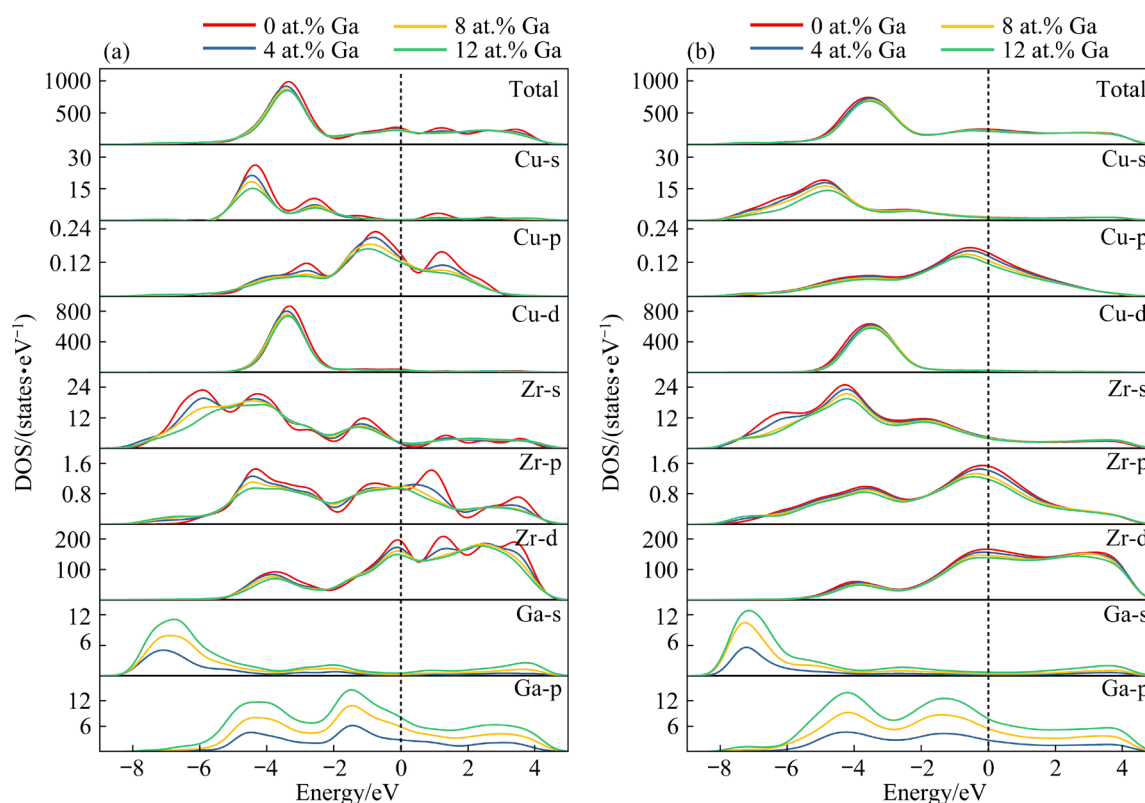
Fig. 7 Total and projected DOS of Ga-doped *B*2-CuZr (a) and amorphous CuZr (b) phases

Cu-s increase in the range from −6 to −8 eV compared to those in the *B*2-CuZr phase, indicating enhanced hybridization between Cu-s and Zr-s. Moreover, the width of the Cu-d PDOS peak in the amorphous CuZr phase is 3.9 eV, which is larger than that of the *B*2-CuZr phase (3.2 eV). The broadening of the Cu-d peak manifests further hybridization between Cu-d and other orbitals. Stronger hybridization induced stronger covalent bonding may explain the higher hardness and strength of the amorphous CuZr phase than those of the *B*2-CuZr phase. On the other hand, the shapes of TDOS and PDOS curves of the amorphous CuZr phase are not significantly changed after Ga doping, which should be the reason for the little changed hardness of the glassy matrix.

To analyze the bonding character and the mechanical behavior of the *B*2-CuZr phase in the MGCs, the effect of one Ga atom substitution of Zr or Cu atom in the *B*2-CuZr phase on the electron density difference distribution in (110) plane is illustrated in Fig. 8. The areas obtaining electrons with blue color are in the interstitial regions of Cu and Zr atoms, which implies the existence of metallic bonding. The shape of the electron density difference map around the Cu atom is nearly circular, while the map around the Zr atom shows a rhombus-like shape (see Fig. 8(a)).

When the Zr atom is substituted by a Ga atom, the shape of the difference charge density map around the Ga atom shows a spherical appearance, while the map around the nearest Zr and Cu atoms has a cherry-like shape and an egg-like shape with a point end toward the Ga atom, respectively (see Fig. 8(b)). Compared to the Zr—Zr bond, the nearest Zr—Ga bond along ⟨001⟩ direction exhibits the transfer of electrons to the Ga atom. Meanwhile, the initial near-rectangular blue areas between two Cu atoms and two Zr atoms change to a "Y" shape after the Ga substitution for Zr. The above results reveal the covalent character of the Zr—Ga bond and the accumulation of electrons around the Ga atom.

For the case of Ga atom replacing Cu atom (see Fig. 8(c)), the electron density difference map around the adjacent Zr atom protrudes slightly toward Ga and Cu atoms, demonstrating the covalent character. On the other hand, the initial near-rectangular blue areas grow lighter, which manifests a lower electron density there. This may result from the Ga atom attracting electrons, because of the higher electronegativity of Ga atom
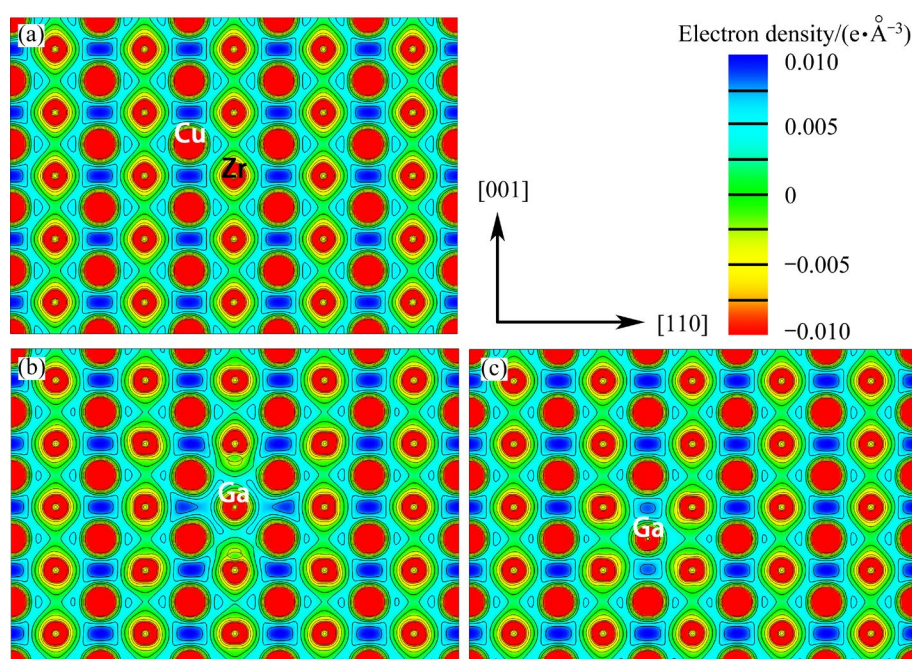
Fig. 8 Electron density difference maps for Ga-doped *B*2-CuZr phases: (a) Pure *B*2-CuZr phase; (b) *B*2-CuZr phase with Ga substituting for Zr; (c) *B*2-CuZr phase with Ga substituting for Cu

than that Zr atom. With the enhanced covalent bonding, the Ga-doped *B*2-CuZr phase will exhibit higher hardness than the pure *B*2-CuZr phase. In addition, the narrowed energy difference between the *B*2-CuZr phase and *B*19′-CuZr phase, and enhanced bonding suppress the martensitic transformation and plastic deformation of the *B*2-CuZr phase, which results in high yield strength of the MGC sample after Ga addition.

4 Conclusions

(1) The GFA of CuZrAlY alloys was improved by adding Ga, which induced the successful synthesis of 10 mm diameter MGCs with single *B*2-CuZr phase reinforcement. Ga doping enhanced the thermal stability of the amorphous CuZr and *B*2-CuZr phases simultaneously.

(2) Ga doping increased hardness of the *B*2-CuZr phase. MGC samples showed work-hardening and pronounced ductility, while the yield stress and strain increased with the growing Ga content.

(3) DFT calculations revealed that Ga addition hindered the martensitic transformation of the *B*2-CuZr phase, and also enhanced covalent bonding which caused elevated hardness of the *B*2-CuZr phase. Furthermore, Ga addition led to lower free energy and stronger orbital hybridization of the amorphous phase, which confirmed the result of

experiments.

CRediT authorship contribution statement

Peng XUE: Conceptualization, Methodology, Investigation, Visualization, Writing − Original draft; **Kun QIAN:** Validation, Writing − Review & editing; **Xiao-bing LI:** Writing − Review & editing; **Lei SHU, Meng-shu ZHANG** and **Jun-jie HAO:** Methodology, Investigation; **Bo CHEN** and **Kui LIU:** Supervision.

Declaration of competing interest

The authors declare that they have no known competing financial interests or personal relationships that could have appeared to influence the work reported in this paper.

References

[1] QIAO J C, WANG Q, PELLETIER J M, KATO H, CASALINI R, CRESPO D, PINEDA E, YAO Y, YANG Y. Structural heterogeneities and mechanical behavior of amorphous alloys [J]. Progress in Materials Science, 2019, 104: 250−329.

[2] HOFMANN D C, SUH J Y, WIEST A, DUAN G, LIND M L, DEMETRIOU M D, JOHNSON W L. Designing metallic

glass matrix composites with high toughness and tensile ductility [J]. Nature, 2008, 451: 1085−1089.

[3]   ZHANG Long, ZHANG Jin-hao, KE Hai-bo, SUN Bao-an, ZHU Zheng-wang, WANG Yan-dong, LI Hong, WANG Ai-min, ZHANG Hai-feng. On low-temperature strength and tensile ductility of bulk metallic glass composites containing stable or shape memory β-Ti crystals [J]. Acta Materialia, 2022, 222: 117444.

[4]   CHEN Yu, TANG Chun-guang, JIANG Jian-zhong. Bulk metallic glass composites containing B2 phase [J]. Progress in Materials Science, 2021, 121: 100799.

[5]   XUE Peng, PAULY S, GAN Wei-min, JIANG Song-shan, FAN Hong-bo, NING Zhi-liang, HUANG Yong-jiang, SUN Jian-fei. Enhanced tensile plasticity of a CuZr-based bulk metallic glass composite induced by ion irradiation [J]. Journal of Materials Science & Technology, 2019, 35: 2221−2226.

[6]   PAULY S, GORANTLA S, WANG G, KÜHN U, ECKERT J. Transformation-mediated ductility in CuZr-based bulk metallic glasses [J]. Nature Materials, 2010, 9: 473−477.

[7]   XUE Peng, HUANG Yong-jiang, JIANG Song-shan, SUN Jian-fei. Cryogenic-temperature-induced phase transformation in a CuZr-based bulk metallic glass composite under tensile stress [J]. Materials Letters, 2020, 262: 127065.

[8]   XUE Peng, HUANG Yong-jiang, PAULY Simon, JIANG Song-shan, GUO Shu, FAN Hong-bo, NING Zhi-liang, CAO Fu-yang, SUN Jian-fei. Quantitatively determining the martensitic transformation in a CuZr-based bulk metallic glass composite [J]. Journal of Alloys and Compounds, 2019, 782: 961−966.

[9]   WU Y, MA D, LI Q K, STOICA A D, SONG W L, WANG H, LIU X J, STOICA G M, WANG G Y, AN K, WANG X L, LI M, LU Z P. Transformation-induced plasticity in bulk metallic glass composites evidenced by in-situ neutron diffraction [J]. Acta Materialia, 2017, 124: 478−488.

[10] HUANG Yong-jiang, XUE Peng, GUO Shu, WU Yang, CHENG Xiang, FAN Hong-bo, NING Zhi-liang, CAO Fu-yang, XING Da-wei, SUN Jian-fei, LIAW P K. Liquid−solid joining of bulk metallic glasses [J]. Scientific Reports, 2016, 6: 30674.

[11] DENG Liang, ZHANG Long, KOSIBA K, LIMBACH R, WONDRACZEK L, WANG Gang, GU Dong-dong, KÜHN U, PAULY S. CuZr-based bulk metallic glass and glass matrix composites fabricated by selective laser melting [J]. Journal of Materials Science & Technology, 2021, 81: 139−150.

[12] YU Ze-jiang, ZHENG Wei, LI Zhi-qiang, LU Yun-zhuo, YUN Xin-bing, QIN Zuo-xiang, LU Xing. Accelerated exploration of TRIP metallic glass composite by laser additive manufacturing [J]. Journal of Materials Science & Technology, 2021, 78: 68−73.

[13] ZHOU S H, NAPOLITANO R E. Phase stability for the Cu−Zr system: First-principles, experiments and solution-based modeling [J]. Acta Materialia, 2010, 58: 2186−2196.

[14] XUE Peng, HUANG Yong-jiang, PAULY S, JIANG Song-shan, GUO Shu, NING Zhi-liang, SUN Jian-fei. Long-term room-temperature aging treatment of a bulk metallic glass composite [J]. Journal of Alloys and Compounds, 2020, 820: 153165.

[15] WANG W H. Roles of minor additions in formation and properties of bulk metallic glasses [J]. Progress in Materials Science, 2007, 52: 540−596.

[16] SONG Wen-li, WU Yuan, WANG Hui, LIU Xiong-jun, CHEN Hou-wen, GUO Zhen-zi, LU Zhao-ping. Microstructural control via copious nucleation manipulated by in situ formed nucleants: Large-sized and ductile metallic glass composites [J]. Advanced Materials, 2016, 28: 8156−8161.

[17] INOUE A, KAWASE D, TSAI A P, ZHANG T, MASUMOTO T. Stability and transformation to crystalline phases of amorphous Zr−Al−Cu alloys with significant supercooled liquid region [J]. Materials Science and Engineering A, 1994, 178: 255−263.

[18] WEN Shu, DAI Cui-ying, MAO Wei-guo, ZHAO Yang, HAN Guo-feng, WANG Xiao-ming. Effects of Ag and Co microalloying on glass-forming abilities and plasticity of Cu−Zr−Al based bulk metallic glasses [J]. Materials & Design, 2022, 220: 110896.

[19] WU D Y, SONG K K, GARGARELLA P, CAO C D, LI R, KABAN I, ECKERT J. Glass-forming ability, thermal stability of B2 CuZr phase, and crystallization kinetics for rapidly solidified Cu−Zr−Zn alloys [J]. Journal of Alloys and Compounds, 2016, 664: 99−108.

[20] DENG Liang, ZHOU Bing-wen, YANG Hong-shuo, JIANG Xin, JIANG Bo-yu, ZHANG Xing-guo. Roles of minor rare-earth elements addition in formation and properties of Cu−Zr−Al bulk metallic glasses [J]. Journal of Alloys and Compounds, 2015, 632: 429−434.

[21] HAO Zi-yan, QIN Kai, SONG Kai-kai, CAO Chong-de. Effect of Fe addition on glass-forming ability, thermal stability of B2 CuZr phase and crystallization kinetics for CuZr-based amorphous alloys [J]. Journal of Materials Research and Technology, 2021, 15: 6464−6475.

[22] LIN Yu-jun, LIN Chao-yu, CAO Zhen-yu, ZHU Mi-xun, ZHANG Jing-jing, CHEN An-fu, PENG Ping, ZHANG Yong, TAN Ming-jen, FU Xiao-ling. Effect of Fe doping on structural, elastic and electronic properties of B2-ZrCu phase under hydrostatic pressure: A first-principles study [J]. Materials Chemistry and Physics, 2021, 272: 124978.

[23] ESCHER B, KABAN I, KÜHN U, ECKERT J, PAULY S. Stability of the B2 CuZr phase in Cu−Zr−Al−Sc bulk metallic glass matrix composites [J]. Journal of Alloys and Compounds, 2019, 790: 657−665.

[24] INOUE A, FAN C, MASUMOTO T. Thermal properties of Zr−TM−B and Zr−TM−Ga (TM=Co, Ni, Cu) amorphous alloys with wide range of supercooling [J]. Materials Transactions, JIM, 1995, 36: 1411−1419.

[25] YU P, BAI H Y, TANG M B, WANG W L. Excellent glass-forming ability in simple Cu$_{50}$Zr$_{50}$-based alloys [J]. Journal of Non-Crystalline Solids, 2005, 351: 1328−1332.

[26] BOKAS G B, LEKKA Ch E, PAPAGEORGIOU D G, EVANGELAKIS G A. Microalloying effects in ternary Cu−Zr−X (X = Be, Mg, Al, Si, P, Nb, Ag) icosahedral clusters and super-clusters from density functional theory computations [J]. Polyhedron, 2017, 133: 1−7.

[27] JIANG Xi-lai, SONG Wen-li, YANG Ming, ZHOU Yuan-bo, HUANG Yan, LU Zhi-chao, ZHANG Yi-bo, DONG Jie, WANG Liang, PENG Bo, HU Chun-ming, ZHAO Jin-kui,

KOU Sheng-zhong, MA Dong. Formation of novel TRIP-ductilized bulk metallic glass composites by manipulating nucleation kinetics via minor alloying [J]. Rare Metals, 2023, 42: 2182−2188.

[28] ZHOU D Q, WU Y, WANG H, HUI X D, LIU X J, LU Z P. Alloying effects on mechanical properties of the Cu−Zr−Al bulk metallic glass composites [J]. Computational Materials Science, 2013, 79: 187−192.

[29] MALEKAN M, RASHIDI R, SHABESTARI S G, ECKERT J. Thermodynamic and kinetic interpretation of the glass-forming ability of Y-containing Cu−Zr−Al bulk metallic glasses [J]. Journal of Non-Crystalline Solids, 2022, 576: 121266.

[30] SOLER J M, ARTACHO E, GALE J D, GARCÍA A, JUNQUERA J, ORDEJÓN P, SÁNCHEZ-PORTAL D. The SIESTA method for ab initio order-N materials simulation [J]. Journal of Physics: Condensed Matter, 2002, 14: 2745−2779.

[31] GARCÍA A, VERSTRAETE M J, POUILLON Y, JUNQUERA J. The PSML format and library for norm-conserving pseudopotential data curation and interoperability [J]. Computer Physics Communications, 2018, 227: 51−71.

[32] PERDEW J P, BURKE K, ERNZERHOF M. Generalized gradient approximation made simple [J]. Physical Review Letters, 1996, 77: 3865−3868.

[33] MOMMA K, IZUMI F. VESTA 3 for three-dimensional visualization of crystal, volumetric and morphology data [J]. Journal of Applied Crystallography, 2011, 44: 1272−1276.

[34] INOUE A. Stabilization of metallic supercooled liquid and bulk amorphous alloys [J]. Acta Materialia, 2000, 48: 279−306.

[35] KISSINGER H E. Reaction kinetics in differential thermal analysis [J]. Analytical Chemistry, 1957, 29: 1702−1706.

[36] SONG K K, PAULY S, ZHANG Y, LI R, GORANTLA S, NARAYANAN N, KÜHN U, GEMMING T, ECKERT J. Triple yielding and deformation mechanisms in metastable $Cu_{47.5}Zr_{47.5}Al_5$ composites [J]. Acta Materialia, 2012, 60: 6000−6012.

[37] XUE Peng, HUANG Yong-jiang, PAULY S, GUO Fang-min, REN Yang, JIANG Song-shan, GUO Fei-ya, GUO Shu, FAN Hong-bo, NING Zhi-liang, SUN Jian-fei. Structural evolution of a CuZr-based bulk metallic glass composite during cryogenic treatment observed by in-situ high-energy X-ray diffraction [J]. Journal of Alloys and Compounds, 2021, 871: 159570.

[38] SONG Kai-kai, WU Shuang, KABAN I, STOICA M, BEDNARČÍK J, SUN Bao-an, CAO Chong-de, WANG Gang, WANG Li, ECKERT J. In situ high-energy X-ray diffraction study of thermally-activated martensitic transformation far below room temperature in CuZr-based bulk metallic glass composites [J]. Journal of Alloys and Compounds, 2020, 841: 155781.

Ga 掺杂对 CuZrAlY 非晶复合材料非晶形成能力及力学性能的影响

薛 鹏，潜 坤，李小兵，陈 波，舒 磊，张孟殊，郝俊杰，刘 奎

季华实验室 材料科学与技术研究部，佛山 528000

摘 要：采用实验与模拟方法研究了 Ga 掺杂对 *B*2-CuZr 相增强大尺寸 CuZrAlY 非晶复合材料结构与力学性能的影响。结果表明，随着 Ga 含量的增加，CuZrAlY 非晶复合材料的非晶形成能力逐渐增强。截面金相及热分析实验证明，Ga 掺杂使晶体相含量降低，合金过冷液相区扩大，并且合金晶化激活能提高。Ga 含量的增加亦使 *B*2-CuZr 相的结构稳定性提高。结构表征和力学性能测试表明，掺杂 Ga 后铸态合金中 *B*19′-CuZr 相消失，同时 *B*2-CuZr 相的马氏体相变得到抑制。采用第一性原理模拟方法阐述了 Ga 掺杂前后 CuZr 基非晶复合材料力学行为的演变机理。上述结果为大尺寸 CuZr 基非晶复合材料的开发与应用奠定了理论基础。

关键词：非晶复合材料；合金化；热学性能；力学性能；密度泛函理论

(Edited by Wei-ping CHEN)